

Revised

H. Schöne, et. al. Dislocation Imaging of an.....

*SAND 97-1840C*  
*SAND--97-1840C*<sup>1</sup>

**Dislocation Imaging of an InAlGaAs Opto-Electronic Modulator using  
IBICC**

*CONF-961120-5*

**Reference number: I - 19**

H. Schöne <sup>a)</sup>, M. B. H. Breese <sup>b)</sup>, S. R. Lee <sup>c)</sup>, R. D. Briggs <sup>c)</sup>, S. A. Casalnuovo <sup>c)</sup>, B. L. Doyle <sup>c)</sup>, T. J. Drummond <sup>c)</sup>, I. J. Fritz <sup>c)</sup>, M. J. Hafich <sup>c)</sup>, G. A. Vawter <sup>c)</sup>

a) Phillips Laboratory, 3550 Aberdeen Ave., Kirtland AFB, Albuquerque, NM 81117

b) Nuclear Physics Laboratory, Keble Rd., Oxford University, Oxford OX1, UK

c) Sandia National Laboratory, P. O. Box 5800, Albuquerque, NM 87185-1056

**RECEIVED**  
**JUL 30 1997**  
**OSTI**

**Abstract**

Sandia is a multiprogram laboratory operated by Sandia Corporation, a Lockheed Martin Company, for the United States Department of Energy under contract DE-AC04-94AL85000.

This paper presents ion beam induced charge collection (IBICC) contrast images showing regions of differing charge collection efficiency within optoelectronic modulator devices. The experiments were carried out at the Sandia nuclear microprobe using 18 MeV carbon and 2 MeV helium ions. Lines of varying densities are observed to run along the different {110} directions which correlate with misfit dislocations within the 392nm thick strained-layer superlattice quantum well of the modulator structure. Independent cross-sectional TEM studies and the electrical properties of the devices under investigation suggest the presence of threading dislocations in the active device region at a density of  $\sim 10^6$  cm<sup>-2</sup>. However, no clear evidence of threading dislocations was observed in the IBICC images as they are possibly masked by the strong contrast of the misfit dislocations. Charge carrier transport within the modulator is used to explain the observed

**DISTRIBUTION OF THIS DOCUMENT IS UNLIMITED**

*ng*

**MASTER**

**DISCLAIMER**

**Portions of this document may be illegible  
in electronic image products. Images are  
produced from the best available original  
document.**

contrast. The different signal to noise levels and rates of damage of the incident ions are assessed.

Correspondence:

Harald Schöne,  
Sandia National Laboratories,  
MS 1056, P.O. Box 5800,  
Albuquerque, NM 87185-1056,  
Tel: (505) 844-2598, Fax: (505) 844-7775,  
email: [hschon@sandia.gov](mailto:hschon@sandia.gov)

## 1. Introduction

Recent improvements in the performance of IR-modulators are attributed to refinements in the growth of high quality strain-relaxed buffer layers which accommodate lattice mismatch between the substrate (GaAs) and the modulator device (nominally  $\text{In}_{0.33}\text{Ga}_{0.67}\text{As}$ ). The buffer was designed to suppress the formation of misfit dislocations and the migration of threading dislocations into the active quantum well region of the modulator. In fact, cross-sectional TEM measurements indicate low dislocation densities within the active device regions. There is, however, no technique currently available to directly image the threading dislocation density that does not require extensive sample preparation. This paper aims to demonstrate Ion Beam Induced Charge Collection (IBICC) as a unique tool to measure and image the extent of dislocations present in deeply buried layers such as strained-layer modulator devices. These IBICC results were interpreted in view of the carrier transport, signal to noise levels, rates of damage and the observed dislocation contrast.

The IBICC technique uses a high energy ( $\sim\text{MeV/amu}$ ) beam at a current of several thousand ions per second focused to a spot size of less than 1 micron, to generate localized electron-hole pairs in semiconductor material. IBICC was developed [1-2] as a means of imaging the depletion regions of microelectronic devices, beneath their thick metallisation and passivation layers. In this study, we attempted to use IBICC to directly image the defect structure of the modulator device.

In previous work [3] IBICC was used to image bands of misfit dislocations present within relaxed silicon-germanium layers grown epitaxially on silicon. This previous experiment was carried out using a 3 MeV proton beam at the Oxford nuclear microprobe.

The inherently low rate of proton energy loss results in small charge pulses that were difficult to resolve from the typical noise level. The resultant low signal to noise ratio limited a more detailed study of the ability of IBICC to image bands of dislocations in semiconductors. We overcame the limitations of this previous work by using focused high-energy beams of carbon and helium ions to give much higher rates of charge carrier generation.

The rate of electronic energy loss (rate of carrier generation) and the rate of nuclear energy loss (rate of nuclear damage) for carbon ions is about 4 times that for helium ions and more than 30 times higher than protons. High atomic number ions with their large carrier generation rate will therefore result in a better signal to noise ratio. The resultant improved signal-to-noise provided by heavy ions must be balanced against the increased defect creation within the scanned area which act as trapping and recombination sites and thereby reduce the collection of charge carriers produced by subsequent ions.

## 2. Experiment

The experiments were performed at Sandia's Nuclear Microprobe facility. An 18 MeV carbon and a 2 MeV helium beam were scanned across an InAlGaAs IR modulator at a beam spot size of typically 1.5 by 0.75  $\mu\text{m}$  and a flux of 1000 to 3000 ions/sec. The size of the region analyzed ranged from 25 by 50  $\mu\text{m}$  to 100 by 100  $\mu\text{m}$ .

The cross section of the tested structure is shown schematically in Fig. 1, and the device is further described in Ref. [4]. The beam-induced charge was collected between the two ohmic contact rings also shown in Fig. 1. The upper and lower mirror stacks were respectively 829 nm and 1622 nm thick, and were comprised of alternating layers of

$\text{In}_{33}\text{Ga}_{67}\text{As}$  and  $\text{In}_{32}\text{Al}_{68}\text{As}$ . The  $n^+$  and  $p^+$  dopant levels in the mirrors vary from a minimum of  $3 \times 10^{17} \text{ cm}^{-3}$  to a maximum of  $3 \times 10^{18} \text{ cm}^{-3}$ . Between these, the intrinsic quantum well structure was 392 nm thick. The surface of the device was capped with a 100 nm thick heavily doped GaAs layer.

Figure 2 shows the results of Monte Carlo Simulations (TRIM) for the electronic energy loss for 18 MeV carbon and 2 MeV helium ions in the tested modulator. The calculated energy loss for helium ions was multiplied by 4 to facilitate easy comparison. The range of both particle species was considerably greater than the thickness of the device structure, so charge carriers were produced throughout all the device layers.

Great care was taken to reduce the noise of the combined system of modulator, wiring and electronics. This minimum level was measured to be equivalent to an r.m.s. noise level of  $0.25 \text{ fC}$ . Each IBICC charge signal was recorded and stored along with the x-y beam position and a time marker. The charge pulses were then processed off-line to produce images showing the median charge pulse height for each beam position. In the IBICC images shown in this paper, dark areas represent regions of small measured charge pulses and light regions represent areas of large measured charge pulses.

By fitting the list mode data, we have found an exponential decrease in the average signal height with beam exposure. The decrease in the charge collected ( $q$ ) as function of ion dose was best fit with  $q = q_0 \exp(-\# \text{ions}/\mu\text{m}^2/813)$  for carbon and  $q = q_0 \exp(-\# \text{ions}/\mu\text{m}^2/2762)$  for helium ions, where  $q_0$  was the initial collected charge. There were no changes in the image features or in the width of the charge distribution with beam exposures discernible. It can be assumed, that a prolonged device irradiation with heavy ions introduces uniformly distributed defects that act as additional charge recombination

or scatter sites which reduce the collected charge accordingly. The charge collected for the images shown have been corrected for the effects of ion beam induced defects to avoid an artificial change in contrast. In other words, we have scaled all the helium and carbon IBICC data to provide images of  $q_0$  versus position.

Three quantities were used to quantify the quality of the IBICC images: 1) minimum resolvable feature size, 2) signal-to-noise ratio, and 3) the contrast of the image. The minimum resolvable feature size was determined by the beam spot size and the lateral diffusion length of minority carriers. We have independently measured the beam spot size to be 1.5 by 0.75  $\mu\text{m}$  for both, the helium and carbon beams. The lateral minority carrier diffusion length was estimated to be about 1.7  $\mu\text{m}$ . By adding the spot size to the diffusion length in quadrature, the minimum resolvable feature size was approximately 2  $\mu\text{m}$  for both the helium and carbon beams. We define the signal to noise ratio of an IBICC image to be the average peak height of the entire image divided by the r.m.s height of the noise. The contrast of an IBICC image was taken to be  $(q_{\max} - q_{\min})/q_{\max}$ , where  $q_{\max}$  ( $q_{\min}$ ) was the maximum (minimum) peak height in the image.

### 3. Results

Figure 3 shows two optical micrographs of a modulator device, in which lines of contrast running along the vertical and horizontal  $\{110\}$  directions can be seen. It was assumed that these lines were related to differences in the epitaxial growth rates caused by

misfit dislocations in the buffer layers which thereby produces a wavy cross-hatched topography at the surface.

Figure 4(a), shows a  $100 \times 100 \mu\text{m}^2$  median filtered IBICC image of the region within box #1 of Fig. 3(b), generated using 18 MeV carbon ions at a fluence of 17 ions/ $\mu\text{m}^2$ . The signal to noise ratio for this image varied from 7:1 with no bias voltage to 15:1 with 1V bias. The contrast for this image was  $\sim 7\%$ . It can be deduced that the cross-hatched structure displayed in the IBICC image was related to the linear features observed in the optical image by comparing of the position and orientation of the vertical line running through the pin-hole in Fig. 3(b) with that in Fig. 4(a).

Figure 4(b) shows a second carbon IBICC image for a different location (see box#2 in Fig. 3(b)). This image was taken with better statistics provided by an increased fluence of 200 ions/ $\mu\text{m}^2$ . A cross-hatch of vertical and horizontal dark lines are running through the image with a contrast between dark and light areas of 17%. The spacing of the vertical lines was 15-20  $\mu\text{m}$  with a line width of 4-5  $\mu\text{m}$ . The observable horizontal line spacing was as small as 4-5  $\mu\text{m}$  with line widths of 3-4  $\mu\text{m}$ . This correlates reasonably well with the observed line spacing in the optical image of 7-10  $\mu\text{m}$  for the vertical and 4.2  $\mu\text{m}$  for the horizontal lines. There was more obvious IBICC contrast from the vertically running lines than from the horizontal lines, whereas in the optical micrographs there was a stronger contrast from lines running horizontally. This could be explained by the fact that the horizontal line density was similar to our minimum resolvable feature size and hence difficult to separate.

The calculated rate of nuclear damage induced by 2 MeV helium ions was 3.5 to 4 times smaller than for 18 MeV carbon. It was expected, that for the same amount of ion

damage we can improve statistics of the IBICC data by a factor of  $\sim 2$  using helium as compared to carbon. Figure 4(c) shows a  $100 \times 50 \mu\text{m}^2$  IBICC image of a new device region generated using  $600 \text{ helium ions}/\mu\text{m}^2$  at 2 MeV, with 1V bias. The signal to noise ratio was reduced in accordance with the smaller energy loss to 3:1 with zero bias and 5:1 at a bias one volt. The improved statistics, however, did not improve the contrast or reveal additional features such as the anticipated dark spots created by threading dislocations. In fact, the contrast was reduced slightly to 14%, possibly showing a larger effect of the increased signal to noise level.

#### 4. Discussion

Charge collection in a modulator is analogous to low level carrier infusion into a P-I-N diode. This charge collection is also quite similar to that exploited in thin fully depleted solid state detectors used as dE spectrometers of particle telescopes. Charge carriers were generated in the intrinsic region of the diode and separated by the self bias and the externally applied field. The generated charge will be registered within the integration time of 1 to 10  $\mu\text{s}$  of a typical charge amplification system used in single ion detection if both electrons on holes were transported to the ohmic contacts. During IBICC analysis of an unbiased modulator, most of the charge is collected from the intrinsic quantum well region, because the very heavily doped mirrors stacks have a drastically reduced minority carrier life time ( $\sim 10$  picosecond) and mobility ( $\sim 1700 \text{ cm}^2/\text{V}\cdot\text{s}$  and  $\sim 130 \text{ cm}^2/\text{V}\cdot\text{s}$  for electrons and holes respectively). The resulting lateral diffusion length calculated with the Einstein relationship in GaAs n-doped at a level of  $3 \times 10^{17} \text{ cm}^{-3}$  is only about 210 nm and 58 nm for the electrons and holes, respectively. The diffusion length in

the vertical direction is further reduced by the multilayered heterostructure, suppressing charge separation and collection from within the mirror stacks.

For reverse bias conditions, the entire voltage drop will form across the intrinsic quantum well region as the resistivity in the heavily doped mirror stack regions is too low (for example n<sup>+</sup>-doped GaAs: 6x10<sup>-3</sup> to 1x10<sup>-3</sup> and p<sup>+</sup>-doped GaAs: 0.09 to 0.01 Ohm-cm) for a significant field gradient to develop. The measured noise level of the detection system was determined to be dominated by the device capacitance. The noise level did not change with reverse bias of up to 3V, indicating that the depletion region does not increase significantly compared to the quantum well thickness. Reverse bias up to 1 V increased the charge signal by 40% over the unbiased case due to the field assisted charge collection; however, it does not change the contrast (typically 10 to 17%) of the observed features. Bias levels above 1V do not improve charge collection, indicating that the saturation velocity is reached at about 25.5 kV/cm. We conclude therefore, that the charge contrast is generated in and limited to the quantum well. This is precisely the region we want to examine with IBICC because only the defects in the quantum well have a significant effect on the electrical/optical performance of the modulator.

The contrast in the IBICC images is believed to originate from misfit dislocations that were located in the quantum well region of the modulator. A misfit dislocation may effect the amount of charge generated by a passing ion (source term) or can reduce the amount of charge detected (sink term) due to charge trapping or scattering. Dislocations can change the magnitude of the ion-induced charge generation by modifying the bandstructure of the InAlGaAs quantum well by inducing local strain fields. However, this effect is not expected to be appreciable. The open bonds of a dislocation core, however,

will clearly act as a trapping center for charge generated by a passing ion (sink term) and to a lesser degree as a charge scattering center. Hence, defect lines reduce the collected amount of charge and lead to the dark lines visible in Fig. (4).

If threading dislocations are present in the quantum well region, they are believed to be observable as pin hole like features at the end of a misfit dislocation line. None of the images revealed any threading dislocation like signatures. We estimate an upper limit for detecting threading dislocations using this IBICC technique to  $10^4/\text{cm}^2$ . At this point it is not clear, if the contrast in IBICC is insufficient for these devices to resolve threading dislocations. As we have demonstrated, using heavy ions for IBICC has the advantage of a much improved signal to noise ratio and a better contrast. It has to be tested if ions with even higher atomic number can improve the charge contrast and possibly reveal the, so far elusive, threading dislocations.

## Figure Captions

Figure 1. Depth profile through the tested modulator device structure.

Figure 2. Monte-Carlo-simulation (TRIM) plots showing the electronic energy loss profiles for 18MeV carbon and 2 MeV helium ions in the InGaAlAs modulator. Note the offset of the stopping power axis and that the helium stopping has been multiplied by 4.

Figure 3. (a),(b) show two optical micrographs of modulator (a) shows the full device area, with the top guard ring and buried contact visible. (b) shows higher magnification of the central. The approximate locations of the IBICC test areas are outlined. The small dots are pin-holes in the surface layers.

Figure 4. (a),(b) Median filtered IBICC image of regions (1) and (2) in Fig. 3(b), generated using 18 MeV carbon ions and corrected for beam damage. (c) Median filtered IBICC image of area (3) in Fig. 3(b) generated using 2 MeV helium ions and corrected for beam damage.

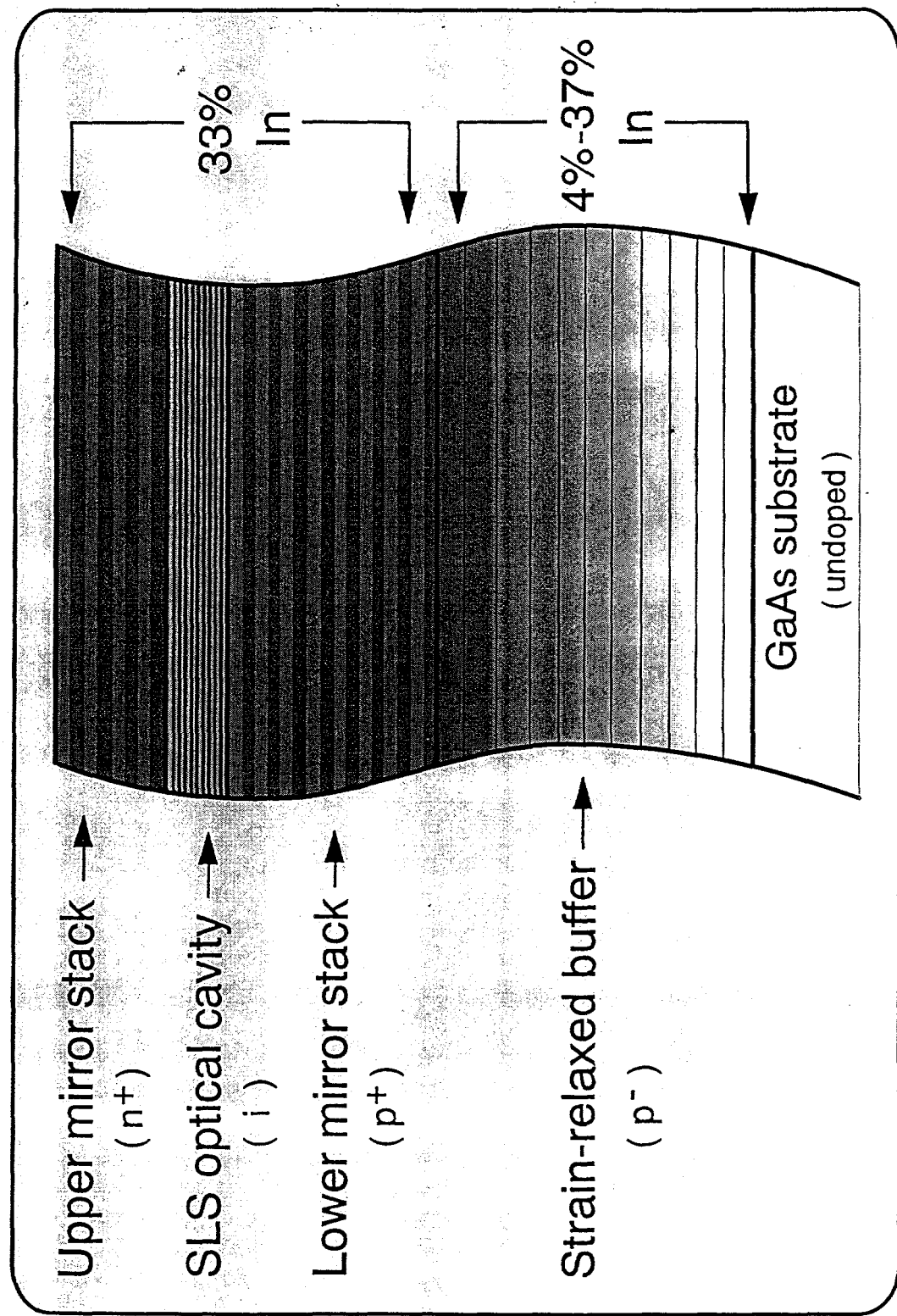
## References

- [1] M B H Breese, G W Grime and F Watt, J. Appl. Phys., 72 (1992) 2097.
- [2] K.M. Horn, B.L. Doyle and F.W. Sexton, J.S. Laird, A. Saint, M. Cholewa, G.J.F. Legge, NIM B77 (1993) 355.
- [3] M.B.H. Breese, P.J.C. King, G.W. Grime, P.R. Wilshaw, Appl. Phys. Lett. 62 (1993) 3309.
- [4] I J Fritz, J A Olsen, A J Howard, T M Brennan, B E Hammons and G A Vawter, IEEE J. Quantum Electronics, 30 (1994) 452.

## DISCLAIMER

This report was prepared as an account of work sponsored by an agency of the United States Government. Neither the United States Government nor any agency thereof, nor any of their employees, makes any warranty, express or implied, or assumes any legal liability or responsibility for the accuracy, completeness, or usefulness of any information, apparatus, product, or process disclosed, or represents that its use would not infringe privately owned rights. Reference herein to any specific commercial product, process, or service by trade name, trademark, manufacturer, or otherwise does not necessarily constitute or imply its endorsement, recommendation, or favoring by the United States Government or any agency thereof. The views and opinions of authors expressed herein do not necessarily state or reflect those of the United States Government or any agency thereof.

Fig. 1



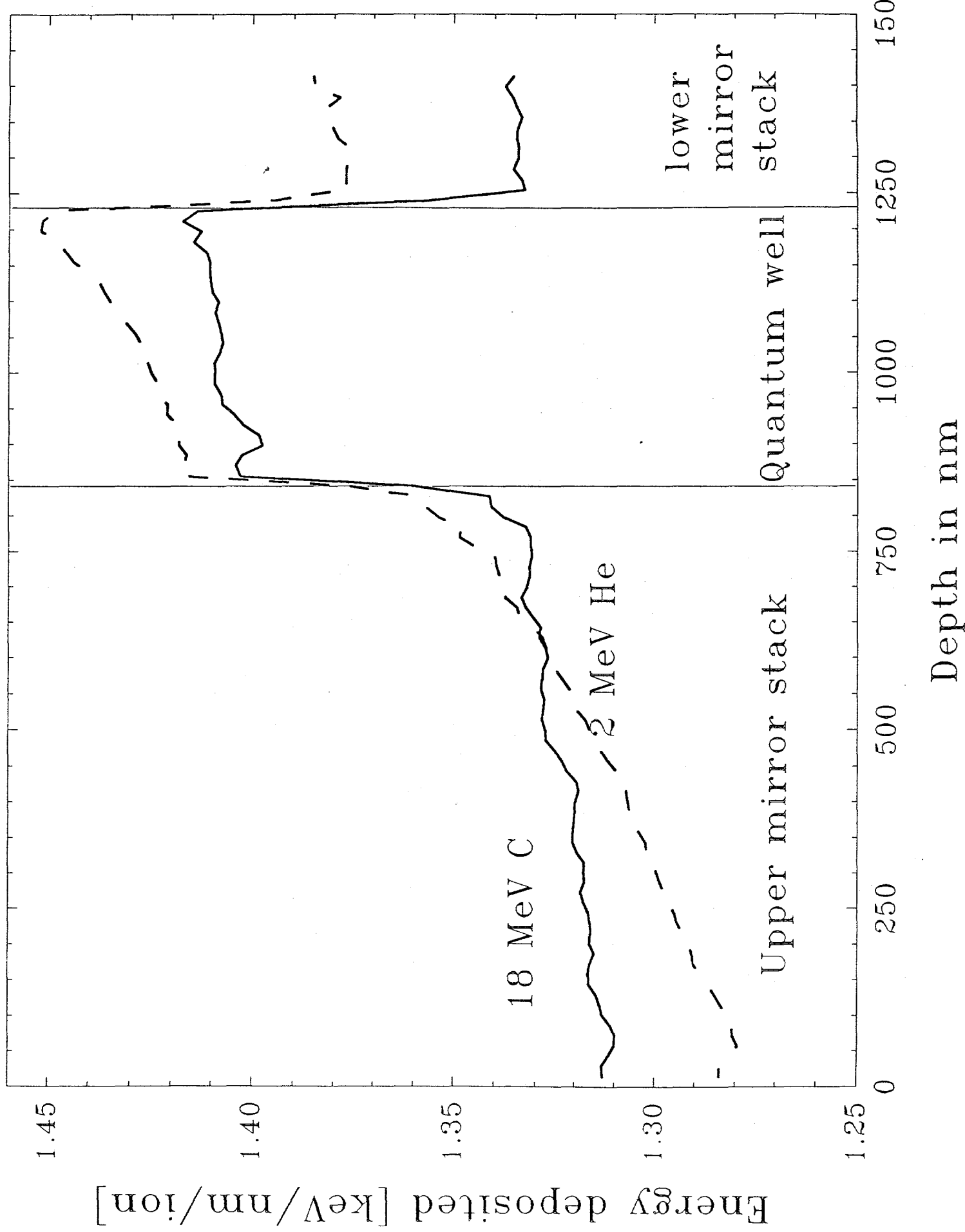
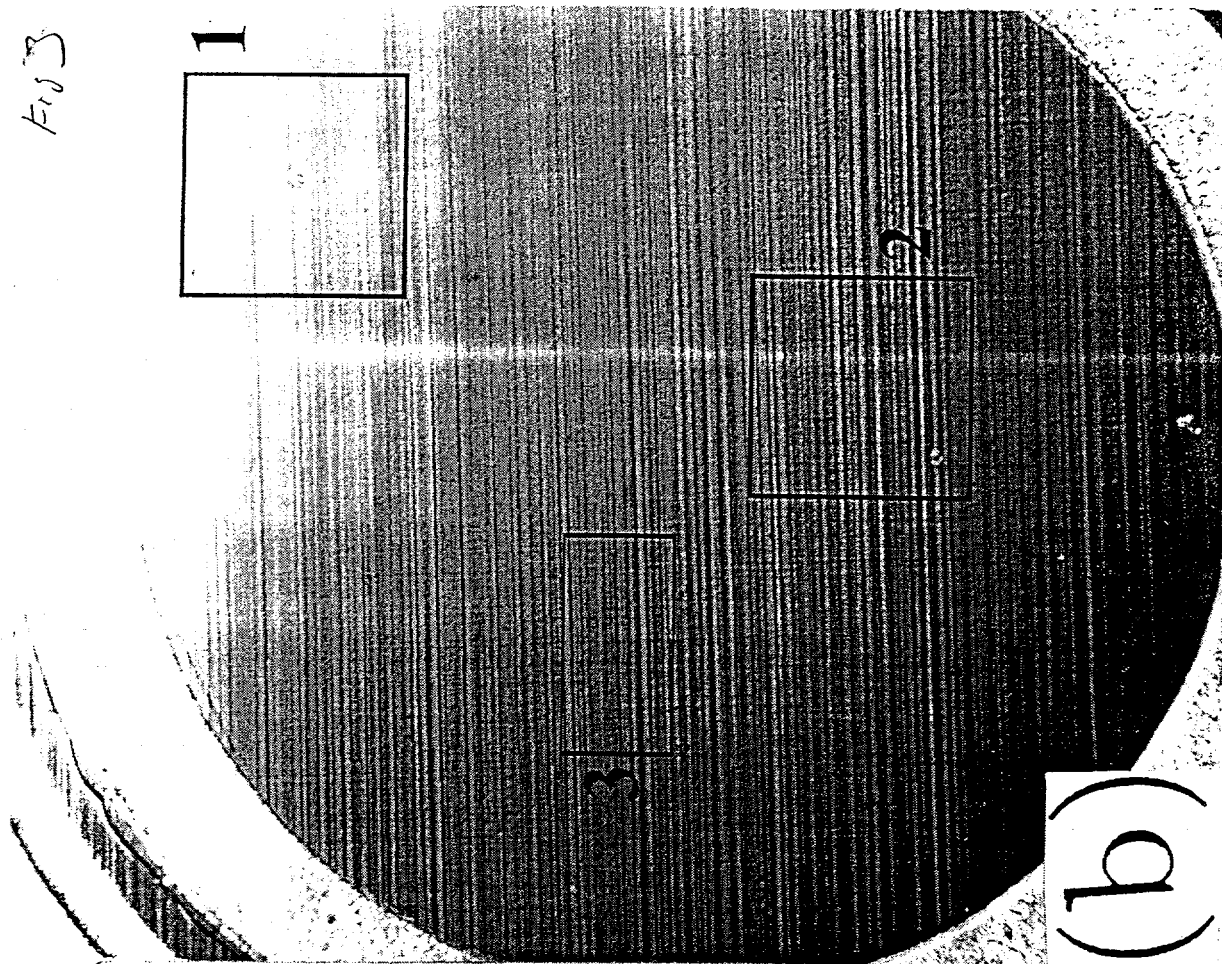
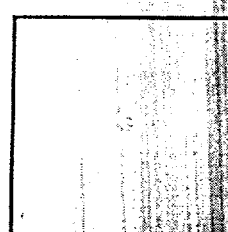


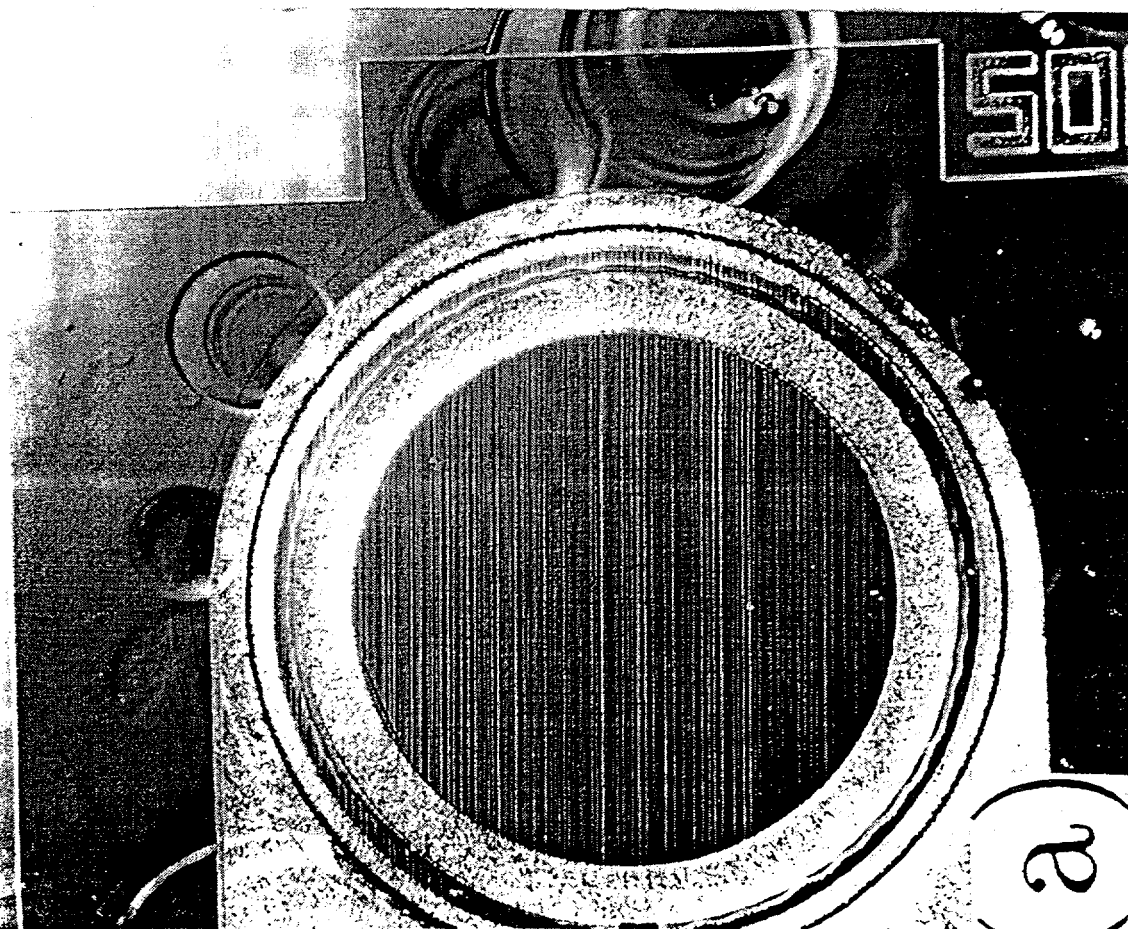
Fig 3

1



2

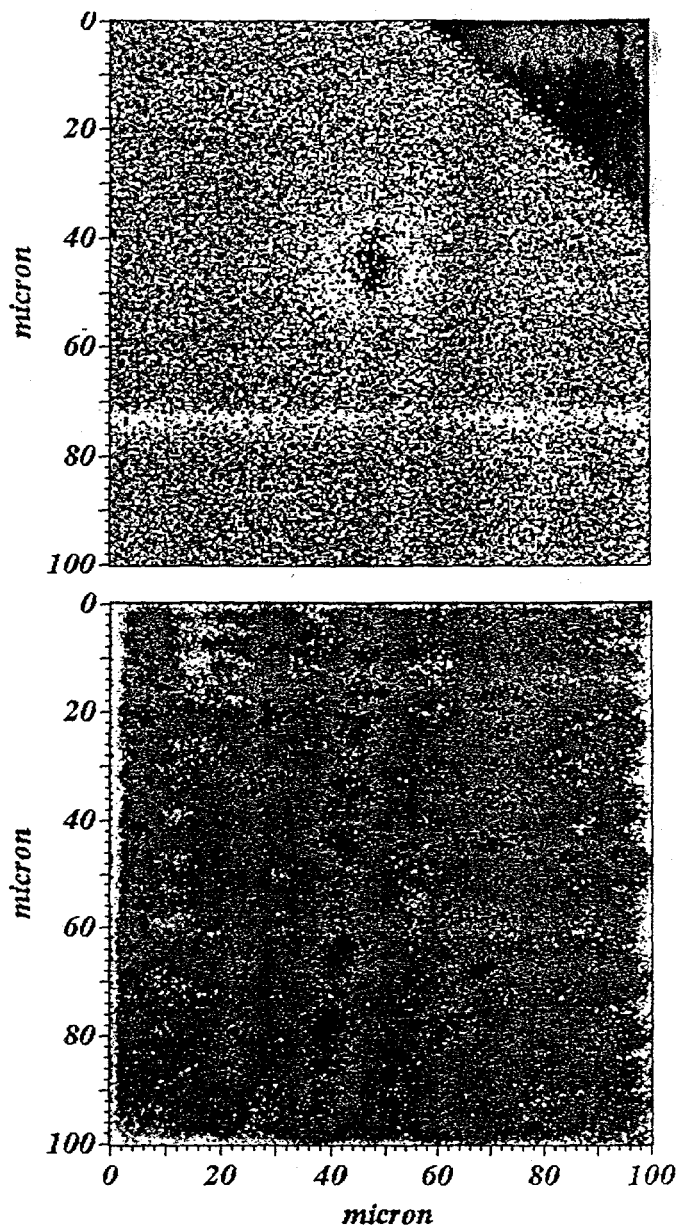
(b)



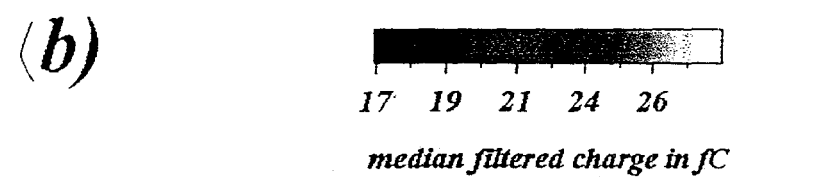
a)

Fig. 4

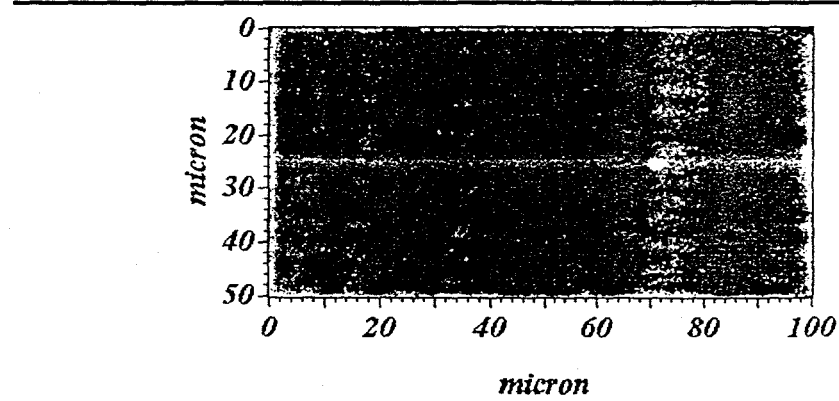
(a)



(b)



median filtered charge in fC



(c)

median filtered charge in fC

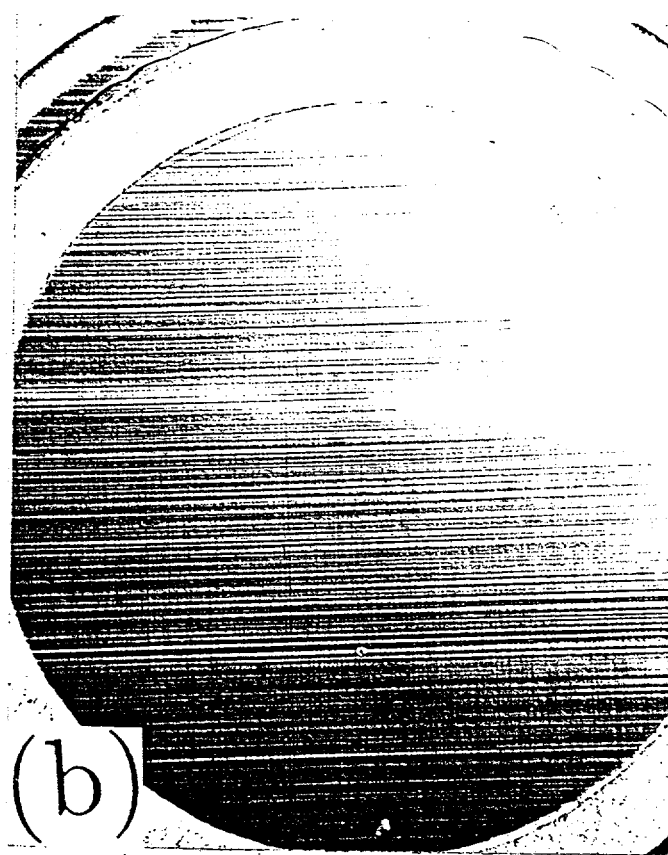
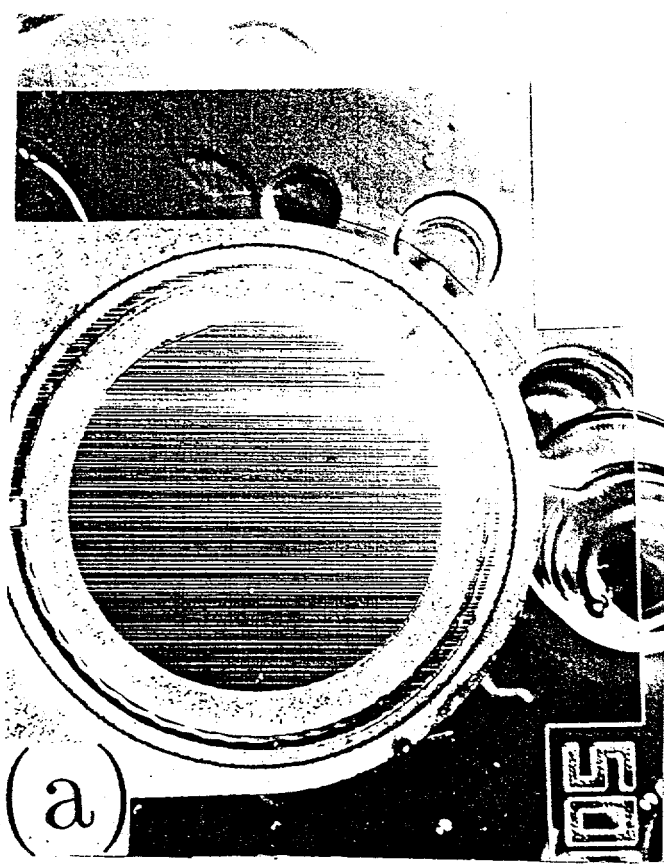


Fig 6

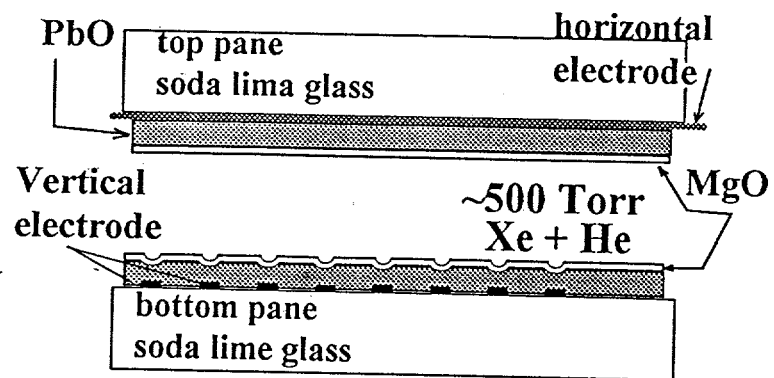
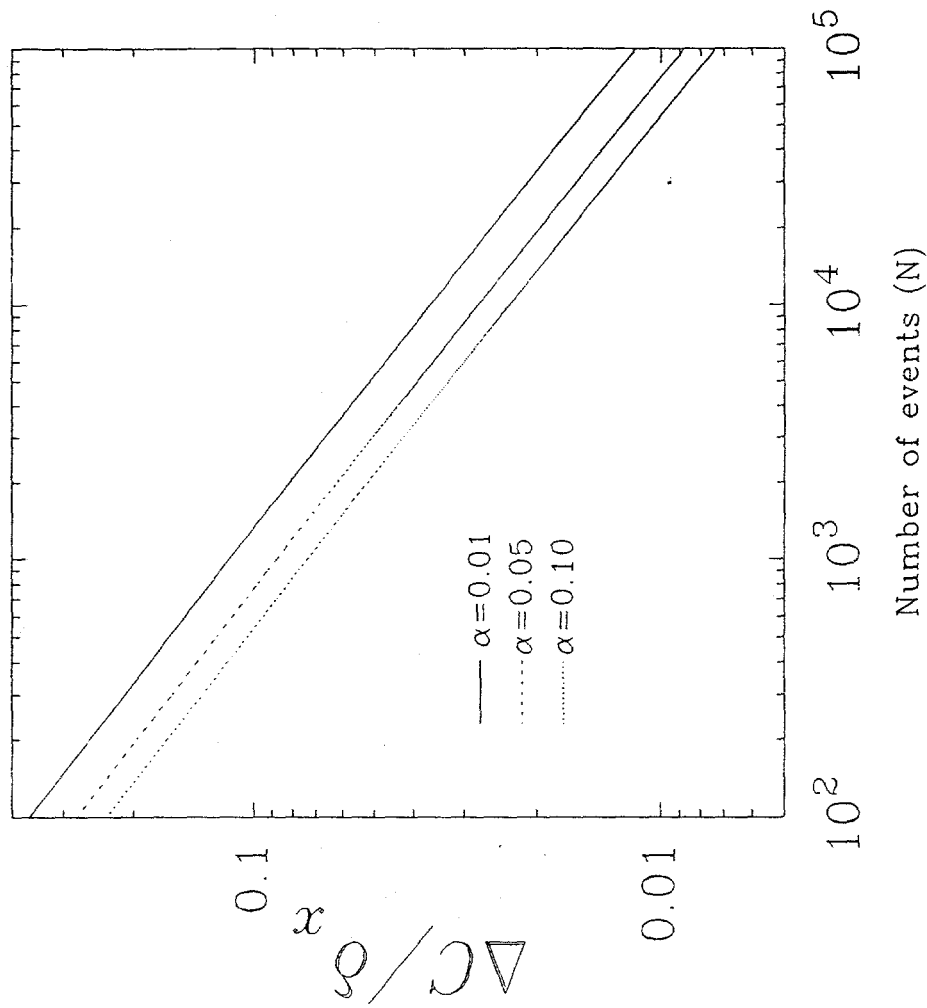


Fig 7



Panel # 1, top pane							
area	ROI	upper left corner [μm]	lower right corner [μm]	# of channel	Comment	MgO [nm]	error [nm]
A	1	0,160	250,250	1536	area to right of electrode	571	±1.1
A	2	59,129	90,137	27	bottom right pixel hump	640	±8.5
A	3	164,133	200,140	30	top right pixel hump	606	±8.0
A	4	74,47	98,55	21	top left pixel hump	658	±9.5
A	5	176,59	200,63	14	bottom left pixel hump	667	±11.3
A	6	59,78	90,98	54	bottom pixel pit	29	±8.0
A	7	164,90	200,109	60	top pixel pit	20	±5.6
A	8	0,0	250,35	576	above electrode	571	±1.8
B	1	0,156	250,250	1600	area to right of electrode	715	±0.7
B	2	117,121	168,129	182	right pixel hump	814	±2.1
B	3	137,59	160,90	63	pixel pit	223	±3.6
C	1	0,176	250,250	1280	area to right of electrode	553	±1.2
C	2	59,94	39,109	35	bottom pixel pit	30	±7.4
C	3	125,106	156,117	36	center pixel pit	34	±7.3
C	4	230,109	238,121	12	top pixel pit	82	±12.6
C	5	16,55	35,63	18	bottom pixel hump	645	±10.3
C	6	133,59	164,74	45	center pixel hump	658	±6.5
C	7	0,0	250,39	640	area to left of electrode	544	±1.7
D	1	0,0	250,78	1280	area left of electrode	546	±1.9
D	2	35,94	74,102	33	bottom left pixel hump	667	±11.6
D	3	138,94	180,105	36	center left pixel hump	640	±11.1
D	4	47,125	74,137	32	bottom pixel pit	1	±11.8
D	5	145,133	176,141	27	center pixel pit	10	±12.8
D	6	39,160	66,168	54	lower right pixel hump	624	±9.1
D	7	145,160	176,168	18	center right pixel hump	615	±15.7
D	8	0,195	250,250	960	area right of electrode	537	±2.1
unaged		0,0	250,250	4096	no structure, entire surface	474	±1.6
Panel # 2, top pane							
A	1	0,0	250,70	1152	area to left of electrodes	526	±1.9
A	2	35,105	63,113	24	lower left pixel hump	631	±13.4
A	3	145,105	168,113	21	center left pixel hump	624	±14.3
A	4	43,145	55,180	40	bottom pixel pit	25	±10.4
A	5	148,145	164,168	35	center pixel pit	20	±11.1
A	6	27,207	63,215	30	lower right pixel hump	674	±12.0
A	7	148,211	176,219	24	center right pixel hump	683	±13.4
unaged		0,0	250,250	4096	no structure, entire surface	495	±1.4
B	-	0,0	250,250	4096	no structure, entire surface	528	±1.1

Table 1: Summary of MgO thickness measurements shown in figure 4 and 5a with 95% confidence value for the error in the depth measurement.